https://doi.org/10.5194/essd-2022-347
Preprint. Discussion started: 23 November 2022

Open Access Earth System Science Data Discussions

A Comprehensive Dataset for Earth System Models in a Permafrost Region: Meteorological, Permafrost, and Carbon Observations (2011–2020) in Northeastern Qinghai-Tibet Plateau

Cuicui Mu [a,b,c*], Xiaoqing Peng [a, b*], Ran Du [a, b], Hebin Liu [a, b], Haodong Jin[a, b], Benben Liang[a, b], Mei Mu [a, b], Wen Sun[a, b], Chenyan Fan [a, b], Xiaodong Wu[d], Oliver W. Frauenfeld[e], Tingjun Zhang[a, b†]

[a] Key Laboratory of Western China's Environmental Systems (Ministry of Education), College of Earth and Environmental Sciences, Lanzhou University, Lanzhou, 730000, China

[b] Observation and Research Station on Eco-Environment of Frozen Ground in the Qilian Mountains, Lanzhou University, Lanzhou 730000, China

[c] Academy of Plateau Science and Sustainability, Qinghai Normal University, Xining, China, 810016

[d] Cryosphere Research Station on the Qinghai–Tibet Plateau, State Key Laboratory of Cryospheric Science, Northwest Institute of Eco-Environment and Resource, Chinese Academy of Sciences, Lanzhou, Gansu 730000, China

[e]Department of Geography, Texas A&M University, College Station, TX 77843-3147, USA

*Corresponding Author: Cuicui Mu (mucc@lzu.edu.cn),
Xiaoqing Peng (pengxq@lzu.edu.cn)

† deceased

https://doi.org/10.5194/essd-2022-347
Preprint. Discussion started: 23 November 2022

Abstract

It's important to understand the role of permafrost in the future climate and water resources management, for huge storage of soil organic carbon and ground ice in the permafrost. To date, large uncertainties still exist in permafrost simulations for many reasons. One reason is being a lack of long-term meteorological, permafrost and carbon observations. Here, we therefore present datasets for air temperatures, precipitation, soil temperature and moisture, active layer thickness, ground temperatures at different depths, soil organic carbon contents, and ecosystem carbon emission rates for the Qilian Mountains of the Northeastern Qinghai-Tibetan Plateau during 2011–2020. The data come from 5 automatic meteorological stations, 21 boreholes with depths from 11.5 to 149.3 m, and 12 active layer monitoring sites, which are used to obtain the hydrothermal and thermal states, and climate change in the study area. Soil organic carbon contents is available from 10 deep boreholes, down to a depth of 20 m. Ecosystem respiration rates are obtained from the prevalent vegetation types of alpine wet meadow, meadow, and steppe for the growing seasons. This decade's high-quality datasets are expected to serve as useful inputs for earth system models, and are for researchers working in those disciplines including geophysics, ecology, and hydrology in alpine environments. The datasets are available from the National Tibetan Plateau/Third Pole Environment Data Center and can be downloaded from http://dx.doi.org/10.11888/Cryos.tpdc.272840 (Mu and Peng, 2022).

1 Introduction

Permafrost underlies approximately 21% of the land area in the Northern Hemisphere (Obu et al., 2019). Sensitive to climate change due to its low temperature, permafrost has important feedbacks to climate change (Cheng et al., 2019; Hugelius et al., 2014; Schuur et al., 2015). Its degradation has been triggered with global permafrost temperature increase (Biskaborn et al., 2019), active layer thickness deepening (Peng et al., 2018), and abruptly collapsing ground (Turetsky et al., 2020). In general, permafrost temperature increases are spatially and temporally very heterogeneous in circumpolar and high-elevation areas. For colder permafrost within

https://doi.org/10.5194/essd-2022-347
Preprint. Discussion started: 23 November 2022

the continuous permafrost zone, permafrost temperature increases have been particularly strong, while warming in the discontinuous permafrost zone has been less pronounced. Relative to warmer, ice-rich permafrost locations, warming has been observed to be greater at colder sites, as well as at those in bedrock or ice-poor sediments (Romanovsky et al., 2010; James et al., 2013; Biskaborn et al., 2019; Smith et al., 2022). Changes in permafrost have greatly influenced hydrological and ecological processes (Vaks et al., 2020; Wang et al., 2020), including changes in vegetation and the net ecosystem carbon balance (McGuire et al., 2018; Mu et al., 2020a).

Because permafrost changes have important effects on many environmental conditions, accurately quantifying and predicting its variability at the regional and hemisphere scales is critical. Modeling permafrost changes has been the focus of many studies, but results have large uncertainties. Different model simulations vary dramatically, e.g., such that permafrost area extent decreases range from 70–99% by the end of 2100 under the RCP8.5 scenario (Guo et al., 2012; Koven et al., 2013; Slater and Lawrence, 2013), and soil temperature estimates at 3.3 m depth vary by as much as 8 °C using different models (Lawrence, 2005). These large uncertainties can be attributable to many reasons, e.g., some models cannot resolve the complex soil hydrothermal processes, or the soil parameters do not have sufficient accuracy, especially in deep layers. Another important reason is a lack of observations. Although the Circumpolar Active Layer Monitoring program and the Global Terrestrial Network for Permafrost include thousands of monitoring sites around the globe, the number of sites and variables still cannot capture the substantial spatial heterogeneity, especially in mountain permafrost regions. Further, observational time series are often not long or continuous enough. Therefore, there is an urgent need for additional and expanded comprehensive permafrost and carbon monitoring networks to better assess regional and global changes in climate and the environment in cold areas, especially in complex, mountainous terrains.

Compared with circum Arctic region, the permafrost on the Qinghai-Tibet Plateau (QTP), also named as the “Third Pole of the Earth,” comprises the largest

https://doi.org/10.5194/essd-2022-347
Preprint. Discussion started: 23 November 2022

permafrost area in the lower middle latitudes (Zou et al., 2017). In contrast with high latitudes, permafrost in this high elevation region is characterized by higher ground temperatures (Cheng et al., 2019), deeper active layers (Hu et al., 2019), and generally an unstable thermal state (Cheng et al., 2019; Ding et al., 2019; Yang et al., 2019). The surface energy balance and the carbon and water cycles over the QTP play an important role in the Asian monsoon, East Asian atmospheric circulation, and in global climate change (Yao, 2017). Therefore, it is particularly important to quantify and understand the current thermal state of permafrost and the analogous carbon feedbacks across this region (Mu et al., 2017; Zhao et al., 2018; Zhao et al., 2021). However, observational monitoring is still challenging in QTP permafrost regions due to its inaccessibility, the complex mountainous terrain, and harsh natural conditions.

The dynamics of water and energy during the freeze-thaw cycle, as well as insulation from peat represent important sources of uncertainty for land surface models simulating permafrost changes (Hu et al., 2016; Yang et al., 2018). Nevertheless, mean annual permafrost temperature trends in the Heihe River basin of the Qilian Mountains on the northern QTP were almost 3.5 times higher (0.48°C/decade) than along the Qinghai-Tibet Highway in the central QTP (0.14°C/decade; Cao et al., 2018; Mu et al., 2020a). The Heihe River basin of the Qilian Mountains in the northern QTP has higher soil organic carbon stocks (Mu et al., 2015; Mu et al., 2016) and experiences dramatic permafrost collapse (Huang et al., 2018; Mu et al., 2020b). Thus, this area is considered a key region for monitoring the permafrost thermal dynamics and interactions between permafrost change and carbon emissions.

The Observation and Research Station on Eco-Environment of Frozen Ground in the Qilian Mountains was established in 2011 and provides a comprehensive permafrost and carbon monitoring network over the upper reaches of the Heihe River basin on the northern QTP. This network primarily monitors permafrost ground temperature, active layer thickness, soil hydrothermal states, snow cover depth, thermokarst development, deep soil organic carbon stocks, and ecosystem carbon emissions (Wang et al., 2015; Peng et al., 2016; Cao et al., 2018; Mu et al., 2017,

https://doi.org/10.5194/essd-2022-347
Preprint. Discussion started: 23 November 2022

2020). It provides important observations for quantifying the hydrothermal mechanisms of permafrost processes and carbon feedbacks based on continuous long-term monitoring and field investigations. This study provides the first synthesis of the northern QTP's meteorology, permafrost thermal state, thermokarst, snow, soil carbon, and ecosystem carbon emissions for the Qilian Mountains. We describe the comprehensive permafrost and carbon monitoring network, evaluate the available data products, and present the free, public data availability and access. These data will provide an important scientific basis for the ecological protection and carbon neutrality of the QTP, and will be a crucial foundation for understanding and evaluating the future response of permafrost to climate change and its feedbacks.

2 Monitoring network

2.1 Location description

China is the country with the third largest permafrost area, with an extent of 1.06×10^6 km^2 located primarily on the QTP (Zou et al., 2017). The Heihe River Basin (98°31'–101°34'E, 37°45'–39°42'N), in the east-central portion of the Qilian Mountains, is the second largest inland river basin in northwest China, located in the northeast of the QTP. Because of the distinctive location, it is a cold semi-arid climate according to the Köppen classification. Characterized by a substantial elevational gradient in soil and vegetation types, the mean annual temperature of the upper reaches of Heihe River varies from 6–10 °C, based on long-term observations (Mu et al., 2013). The annual precipitation amount ranges 250–750 mm (Zhao et al., 2005). The network area is characterized not only by extensive permafrost, but also by widespread seasonally frozen ground with a maximum seasonal freeze depth of more than 2.5 m (Peng et al., 2016).

The network is primarily distributed in two regions: Yeniugou and Eboling. Boreholes were established starting in 2011, and of the current total of 21 (18 in Yeniugou, and 3 in Eboling), 15 are in permafrost and 6 in seasonally frozen ground

https://doi.org/10.5194/essd-2022-347
Preprint. Discussion started: 23 November 2022

Open Access Earth System Science Data Discussions

(Figure 1, Table 1). Most boreholes became operational between 2011 and 2014, with 3 more added in 2019. Yeniugou and Eboling have similar climatic conditions, but permafrost characteristics in the two regions vary due to differences in slope, soil, vegetation, peat, soil moisture content, and snow cover (Du et al., 2022). The soil parent material is alluvium, and most sites are located in a mountain basin with a gradual slope, with two sites (EBoA and EBoB; see Table 1) in a mountain valley. The primary vegetation types are alpine wetland, alpine meadow, alpine steppe, and alpine desert steppe. There are rich peat layers at the Eboling sites. The seasonally frozen ground boreholes are all in Yeniugou. In these boreholes, we also installed automatic weather stations and collected active layer observations.

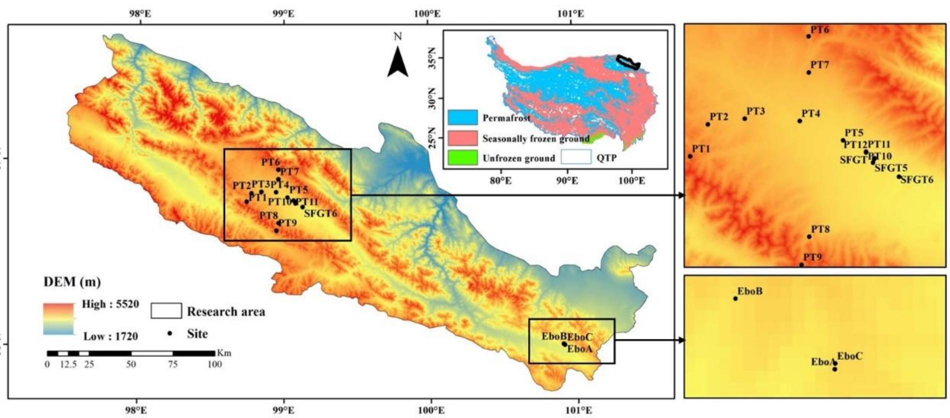

Figure 1 The monitoring network of frozen ground, active layer, and meteorological sites over the Heihe River basin in the northeastern Qinghai-Tibetan Plateau. Some sites are included one, or two or three types observations. The detail can be seen the tables in each variables.

Table 1 Description of boreholes for permafrost and seasonally frozen ground (SFG) observations. Start date is the year when monitoring began. The observation types include frozen ground temperature (type a), active layer hydro-thermal (type b), and meteorological variables (type c).

ID	Name	Longitude (°E)	Latitude (°N)	Elevation (m)	Depth (m)	Ground Type	Start Date	Observation Type
1	PT1	98.75	38.78	4132	100	Permafrost	2011	a, b ,c
2	PT2	98.78	38.83	3987	69	Permafrost	2011	a
3	PT3	98.85	38.84	3843	50	Permafrost	2011	a, b

https://doi.org/10.5194/essd-2022-347
Preprint. Discussion started: 23 November 2022

4	PT4	98.95	38.83	3775	90.3	Permafrost	2011	a, b
5	PT5	99.03	38.81	3700	20.4	Permafrost	2011	a, b ,c
6	PT6	98.96	38.95	4158	50	Permafrost	2014	a, b ,c
7	PT7	98.96	38.90	3956	36	Permafrost	2014	a, b
8	PT8	98.96	38.67	3886	50	Permafrost	2014	a, b
9	PT9	98.95	38.63	4138	149.3	Permafrost	2014	a, b ,c
10	PT10	99.07	38.79	3681	20	Permafrost	2014	a, b
11	PT11	99.07	38.79	3681	20	Permafrost	2019	a
12	PT12	99.07	38.79	3680	20	Permafrost	2014	a
13	EboA	100.92	38.00	3691	20	Permafrost	2012	a ,b, c
14	EboB	100.91	38.00	3615	11.5	Permafrost	2012	a ,b
15	EboC	100.92	38.00	3691	20	Permafrost	2019	a
16	SFGT	99.07	38.79	3680	20	SFG	2014	a ,b
17	SFGT3	99.08	38.78	3662	20	SFG	2014	a
18	SFGT4	99.08	38.78	3658	20	SFG	2014	a
19	SFGT5	99.08	38.77	3642	20.7	SFG	2011	a
20	SFGT6	99.13	38.75	3609	20	SFG	2011	a
21	SFGT7	99.07	38.79	3680	20	SFG	2019	a

2.2 Variables

2.2.1 Borehole monitoring

Before choosing the locations for borehole sites, we carefully considered the factors that affect the thermal state of permafrost. The depths of the boreholes range from 11.5 to 149.3 m. Each borehole is numbered, and the boreholes located on permafrost are named PT1 to PT11. The boreholes located in seasonally frozen ground are numbered SFGT–SFGT7. Metal pipes with a thickness of 70 mm were placed in each borehole, and the gap between the pipe wall and the borehole was backfilled with the original soil from each borehole. Each borehole was equipped with a thermistor chain customized by the State Key Laboratory of Frozen Soil Engineering, Chinese Academy of Sciences, to measure deep ground temperatures with an accuracy of ± 0.05 °C (Figure 2). Generally, the observation intervals are 0.2 m between 0–2 m, 0.5 m between 2–5 m, 1 m between 5–10 m, 2 m between 10–20 m, and 5 m between 20–50 m. Before 2019, most boreholes were manually measured every 2–3 months (Table 3). Several boreholes were equipped with automated data loggers after 2019, to obtain continuous measurements from then on.

https://doi.org/10.5194/essd-2022-347
Preprint. Discussion started: 23 November 2022

Open Access Earth System Science Data Discussions

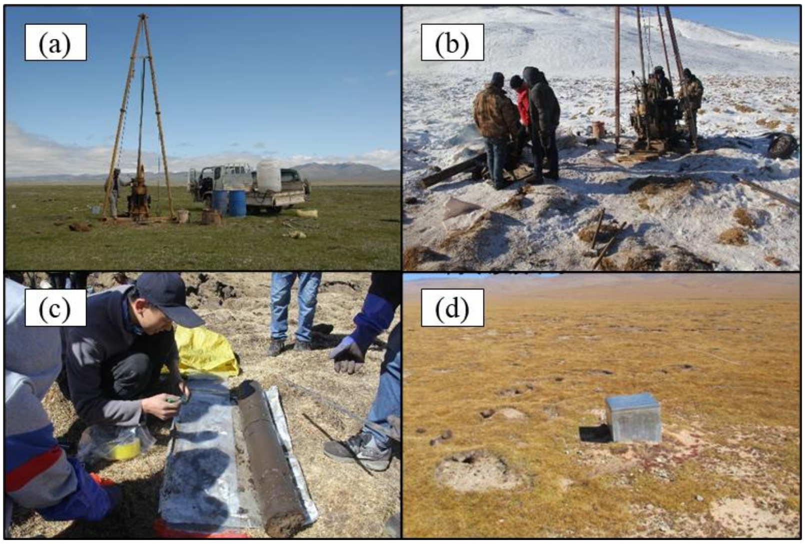

Figure 2 Permafrost drilling in the field during (a) spring and (b) winter, (c) subsurface core sample collection, and (d) a protective chamber for a ground temperature borehole.

Table 2 Measurement depths and data collection methods at the monitoring sites. These sites are for the ground temperature in each depth.

Name	Depth (m)	Collection method
PT1	4.0, 5.0, 6.0, 7.0, 8.0, 10.0, 12.0, 15.0, 18.0, 21.0, 25.0, 30.0, 40.0, 45.0, 50.0, 55.0, 60.0, 65.0, 70.0, 75.0, 80.0, 85.0,90.0, 95.0, 100.0	manual
PT2	0.0, 0.2, 0.4, 0.6, 0.8, 1, 1.2, 1.4, 1.6, 1.8, 2, 2.2, 2.4, 2.6, 2.8, 3, 3.5, 4.0, 5.0, 6.0, 7.0, 8.0,10.0, 12.0,14.0, 16.0, 18.0, 23.0, 28.0, 33.0, 38.0, 43.0, 48.0, 53.0, 58.0, 63.0, 67.0	manual
PT3	2.0, 2.2, 2.4, 2.6, 2.8, 3.0, 3.2, 3.4, 3.6, 3.8, 4.0, 4.2, 4.4, 4.6, 4.8, 5.0, 5.5, 6.0, 7.0, 8.0, 9.0, 10.0,12.0, 14.0, 16.0, 18.0, 20.0, 25.0, 30.0, 35.0, 40.0, 45.0, 50.0	manual (10/9/2011–4/10/2019) automatic (4/12/2019–present)
PT4	2.0, 2.2, 2.4, 2.6, 2.8, 3.0, 3.2, 3.4, 3.6, 3.8, 4.0, 4.2, 4.4, 4.6, 4.8, 5.0, 5.5, 6.0, 7.0, 8.0, 9.0, 10.0,12.0, 14.0,16.0, 18.0, 20.0, 25.0, 30.0, 35.0, 40.0, 45.0, 50.0	manual (10/18/2011–4/10/2019) automatic (4/12/2019–present)
PT5	2.0, 2.5, 3.0, 3.5, 4.0, 4.5, 5.0, 6.0, 7.0, 8.0, 10.0, 12.0, 14.0, 16.0, 18.0, 20.0	manual
PT6	2.0, 2.5, 3.0, 3.5, 4.0, 4.5, 5.0, 6.0, 7.0, 8.0, 9.0, 10.0, 12.0, 14.0, 16.0, 18.0, 20.0, 25.0, 30.0, 35.0, 40.0, 45.0, 50.0	manual (7/12/2014–10/16/2020) automatic (10/18/2020–present)
PT7	2.0, 2.5, 3.0, 3.5, 4.0, 4.5, 5.0, 6.0, 7.0, 8.0, 9.0,	manual

https://doi.org/10.5194/essd-2022-347
Preprint. Discussion started: 23 November 2022

	10.0, 12.0, 14.0, 16.0, 18.0, 20.0, 22.0, 24.0, 26.0, 28.0, 32.0, 36.0	
PT8	2.0, 2.5, 3.0, 3.5, 4.0, 4.5, 5.0, 6.0, 7.0, 8.0, 9.0, 10.0, 12.0, 14.0, 16.0, 18.0, 20.0, 25.0, 30.0, 35.0, 40.0, 45.0, 50.0	manual
PT9	1.3, 1.8, 2.3, 2.8, 3.3, 3.8, 4.3, 5.3, 6.3, 7.3, 8.3, 9.3, 10.3, 11.3, 12.3, 13.3, 14.3, 16.3, 19.3, 23.3, 29.3, 34.3, 39.3, 44.3, 49.3, 54.3, 59.3, 64.3, 69.3, 74.3, 79.3,84.3, 89.3, 99.3, 104.3, 109.3, 114.3, 119.3, 129.3, 139.3, 149.3	manual (7/12/2014–10/15/2020) automatic (10/17/2020–present)
PT10	2.0, 2.5, 3.0, 3.4, 4.0, 4.4, 4.6, 4.8, 5.0, 5.4, 5.8, 6.0, 7.0, 8.0, 9.0, 10.0, 11.0, 12.0, 13.0, 13.4, 13.6, 13.8, 14.0, 14.2, 14.4, 14.6, 15.0, 16.0, 17.0, 18.0, 19.0, 20.0	automatic
PT11	0.1, 0.5, 1.0, 1.5, 2.0, 2.5, 3.0, 3.5, 4.0, 4.5, 5.0, 5.5, 6.0, 7.0, 8.0, 9.0, 10.0, 11.0, 12.0, 13.0, 14.0, 15.0, 16.0, 18.0, 20.0	manual
PT12	2.0, 2.5, 3.0, 3.5, 4.0, 4.5, 5.0, 6.0, 7.0, 8.0, 9.0, 10.0, 12.0, 14.0, 15.0, 16.0, 17.0, 18.0, 19.0, 20.0	automatic
EboA	1.0, 1.5, 2.0, 2.5, 3.0, 3.5, 4.0, 5.0, 6.0, 7.0, 9.0, 11.0, 13.0, 15.0, 17.0, 19.0	manual
EboB	0.2, 0.4, 0.6, 0.8, 1.0, 1.2, 1.4, 1.6, 1.8, 2.0, 2.5, 3.0, 4.0, 5.0, 6.0, 8.0, 10.0, 11.5	manual
EboC	1.0, 1.5, 2.0, 2.5, 3.0, 3.5, 4.0, 4.5, 5.0, 5.5, 6.0, 7.0, 8.0, 9.0, 10.0, 11.0, 12.0	manual
SFGT	2.0, 2.5, 3.0, 3.5, 4.0, 4.5, 5.0, 5.5, 6.0, 7.0, 8.0, 9.0, 10.0, 11.0, 12.0, 13.0, 14.0, 15.0, 16.0, 17.0, 18.0, 19.0, 20.0	automatic
SFGT3	2.0, 2.5, 3.0, 3.5, 4.0, 4.5, 5.0, 6.0, 7.0, 8.0, 9.0, 10.0, 12.0, 14.0, 16.0, 18.0, 20.0	manual
SFGT4	2.0, 2.5, 3.0, 3.5, 4.0, 4.5, 5.0, 6.0, 7.0, 8.0, 9.0, 10.0, 12.0, 14.0, 16.0, 18.0, 20.0	manual
SFGT5	2.0, 2.5, 3.0, 3.5, 4.0, 4.5, 5.0, 6.0, 7.0, 8.0, 10.0, 12.0, 14.0, 16.0, 18.0, 20.0	manual
SFGT6	2.0, 3.0, 3.5, 4.0, 4.5, 5.0, 6.0, 7.0, 8.0, 14.0, 16.0, 18.0, 20.0	manual
SFGT7	0.1, 0.5, 1.0, 1.5, 2.0, 2.5, 3.0, 3.5, 4.0, 4.5, 5.0, 5.5, 6.0, 7.0, 8.0, 9.0, 10.0, 11.0, 12.0, 13.0, 14.0, 15.0, 16.0, 18.0, 20.0, 22.0	manual

2.2.2 Comprehensive meteorological system

Five sites in the study area (EBoA, PT1, PT5, PT6 and PT9) are equipped with a comprehensive meteorological system that collects: radiation (Kipp & Zonen CNR4 Net Radiometer), air temperature and relative humidity (Campbell Scientific HMP155A), wind speed and direction (Campbell Scientific 05103-45-L Wind Monitor, Alpine Version), precipitation (Geonor T-200B gauge), atmospheric pressure (Campbell Scientific CS106 barometer by Vaisala), and other variables (Figure 3a). All instruments were placed at a 2.0 m height, and data are collected by a

https://doi.org/10.5194/essd-2022-347
Preprint. Discussion started: 23 November 2022

Campbell Scientific CR1000 data logger every 30 minutes. Upward/downward shortwave and longwave radiation measured by the CNR4 have an accuracy of 1%. The accuracy of air temperature and relative humidity are 0.2 ℃ and ±1.7%, respectively. Wind speed from the 05103-45-L has an accuracy of ±0.3 m/s, and the accuracy of precipitation is about ±0.1 mm. Finally, the accuracy of atmospheric pressure is approximately ±2.0 hPa (−40 ℃–60 ℃). Detailed information about the instruments is shown in Table 3.

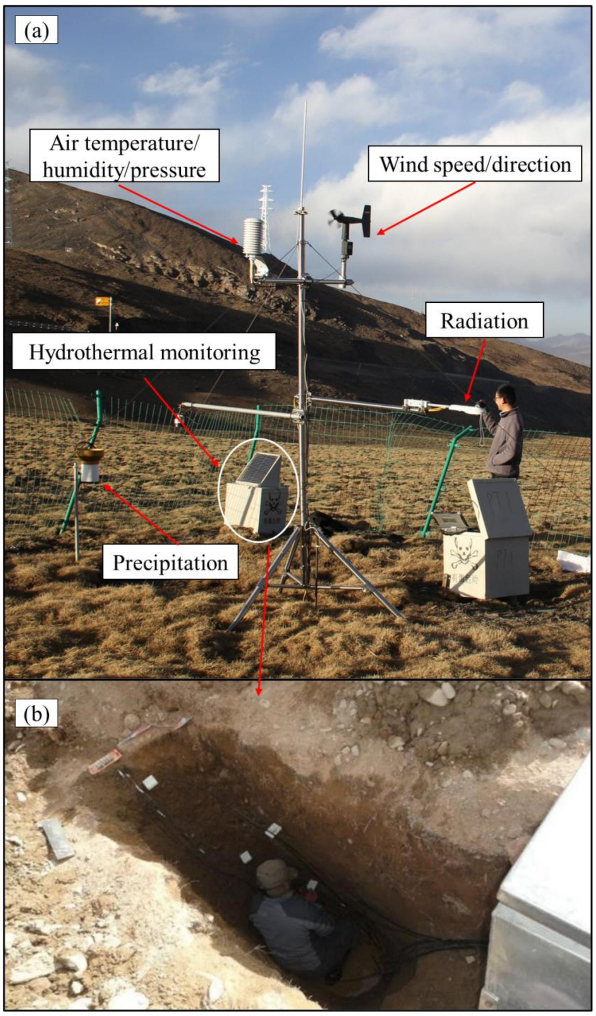

Figure 3 The meteorological monitoring parameters including (a) wind speed and direction, air

https://doi.org/10.5194/essd-2022-347
Preprint. Discussion started: 23 November 2022

temperature/humidity/pressure, radiation, precipitation, and (b) soil temperature and moisture monitoring equipment.

Table 3 Summary of observing-site sensors and information for the meteorological data, ground temperature, and soil moisture and temperature of the active layer.

Monitoring indicators	Available sites	Observation item	Instruments	Accuracy	Height	Frequencies
Meteorological observation	5	Upward/downward shortwave radiation	CNR4, Kipp&Zonen, Netherlands	1%	2.0 m	30 minutes
		Upward/downward longwave radiation			2.0 m	30 minutes
		Air temperature	HMP155A, Vaisala Finland	±0.2 °C	2.0 m	30 minutes
		Air humidity		±1.7%	2.0 m	30 minutes
		Wind velocity	05103-45-L Campbell, USA	±0.3 m/s	2.0 m	30 minutes
		Precipitation	T-200B precipitation gauge	±0.1 mm	2.0 m	30 minutes
		Atmospheric pressure	CS106	±2.0 hPa (−40°C to +60°C)	2.0 m	30 minutes
Soil state of the active layer	12	Soil temperature	109 thermocouple temperature	±0.2 °C	/	30 minutes
		Soil moisture content	CS616 soil moisture sensor	±2.5%	/	30 minutes
Borehole (automatic)	7	Ground temperature	Thermistor SKLFSE, China	±0.05 °C	/	1 day
Borehole (manual)	18	Ground temperature	Thermistor SKLFSE, China	±0.05 °C	/	Irregular

2.2.3 Hydrothermal monitoring of the active layer

There are 12 sites with observations of the hydrothermal state of the active layer (Table 4 and Figure 3b). Soil temperature is monitored using a Campbell scientific 109 sensor probe, with an accuracy of ±0.03 °C and a measurement range of −50 °C to 70 °C. Soil moisture is measured as volumetric water content using a CS616 water content reflectometer with an accuracy of ±2.5%, and a working environment from −50 °C to 70 °C. The soil temperature and moisture sensors are connected to a data logger and record every 30 minutes. The soil temperature sensors are installed at depths of 5, 10, 20, 40, 80, 100, 120, 140, 160, 180 and 200 cm. The soil moisture sensors are installed at the depths of 20, 40, 80, 120, 160 and 180 cm (Table 4).

Table 4 Soil temperature and moisture monitoring in the active layer. Date refers to the starting

https://doi.org/10.5194/essd-2022-347
Preprint. Discussion started: 23 November 2022

year of monitoring.

Name	Date	Variable	Depth (cm)
PT1	2012	Soil temperature	5, 10, 20, 40, 80, 100, 120, 140, 160, 180
		Soil moisture	40, 80, 120, 160
PT3	2012	Soil temperature	5, 10, 20, 40, 80, 100, 120, 160, 200
		Soil moisture	40, 80, 120, 180
PT4	2012	Soil temperature	5, 10, 20, 40, 60, 80, 120, 160, 200
		Soil moisture	20, 60, 100, 136
PT5	2012	Soil temperature	5, 10, 20, 40, 60, 80, 120, 140
		Soil moisture	15, 20, 40, 60, 80
PT6	2017	Soil temperature	5, 10, 20, 40, 80, 120, 160, 170
		Soil moisture	20, 40, 80, 160
PT7	2021	Soil temperature	10, 20, 40, 80
		Soil moisture	10, 20, 40, 80
PT8	2021	Soil temperature	10, 20, 40, 80
		Soil moisture	10, 20, 40, 80
PT9	2014	Soil temperature	5, 10, 20, 40, 60, 80, 100
		Soil moisture	20, 40, 60, 80
PT10	2014	Soil temperature	5, 10, 20, 40, 60, 80, 120, 160, 180
		Soil moisture	40, 80, 120, 180
SFGT	2014	Soil temperature	10, 40, 80, 120, 160
		Soil moisture	40, 80, 120, 160
EboA	2012	Soil temperature	5, 10, 20, 40, 60, 77
		Soil moisture	5, 10, 20, 40, 60
EboB	2014	Soil temperature	5, 10, 20, 40
		Soil moisture	5, 10, 20, 40

2.6 Soil organic carbon stocks

Ten deep boreholes in both permafrost and seasonally frozen ground are available for measurements of soil organic carbon content in the upper reaches of the Heihe River Basin. These boreholes were drilled at elevations of 3,615–4,138 m, where the soil parent materials is alluvium. Additional geographic information for these boreholes is shown in Table 5.

https://doi.org/10.5194/essd-2022-347
Preprint. Discussion started: 23 November 2022

The depth of each borehole is approximately 20 m (Table 1), and the cores collected at each site were approximately 15 cm in diameter. The depths of the collected samples at PT6, PT9, EboA, and EboB were 9.0, 7.0, 6.0, and 5.0 m, respectively, because of rock layers below these depths. For PT12, no soil samples in the upper 2 m were possible because of high gravel content. For all other sites, each 30–40-cm-long drilled core was photographed, wrapped, labeled, and stored in a freezer at −20 °C. Upon returning to the laboratory at Lanzhou University, the samples were transferred to an ultralow-temperature freezer.

Table 5 Soil organic carbon content boreholes.

Site	Aspect	Slope (°)	Topography	Vegetation type	Dominant species
PT4	flat	flat	piedmont plain	Alpine meadow	*Kobresia pygmaea* C. B. Clarke
PT5	flat	flat	piedmont plain	Alpine meadow	
PT6	southeast	2	piedmont slope	Alpine meadow	*Ajania tibetica*
PT7	northeast	1.5	piedmont plain	Alpine meadow	*Rhodiola subopposita*
PT9	eastern	2	piedmont slope	Alpine wet meadow	*K. tibetica Maxim.*
PT10	flat	flat	piedmont plain	Alpine steppe	*K. humilis* (C. A. Mey.) Serg.
PT11	flat	flat	piedmont plain	Alpine steppe	
PT12	flat	flat	piedmont plain	Alpine steppe	
EboA	northwest	1.2	piedmont slope	Alpine wet meadow	*K. tibetica Maxim.*
EboB	northwest	2.5	piedmont slope	Alpine meadow	*K. tibetica Maxim.*

2.7 Monitoring of ecosystem carbon emissions

Ecosystem respiration and net ecosystem carbon exchange (NEE) for three vegetation types—alpine wet meadow (AWM), alpine meadow (AM), and alpine steppe (AS)—were monitored at ten sites in June, July, August, and September or October from 2014 to 2016. To exclude differences in vegetation and micro-landforms, relatively flat areas were selected and regions with patchy vegetation distributions were not considered. We fenced 20 × 20 m blocks to keep out ungulate grazers and, within these blocks, we applied a paired design with three-time replication (Figure 4).

https://doi.org/10.5194/essd-2022-347
Preprint. Discussion started: 23 November 2022

Figure 4 Measurements of ecosystem respiration using an LI-8100 Soil CO_2 Flux System. The round collar is connected to the automated chamber (opaque).

3 Data processing and analysis

3.1 Climate and frozen ground data

Based on daily observations, the full record is used to calculate seasonal average temperature, annual average temperature, and seasonal total precipitation since 2014. Because soil temperature and moisture are measured every 30 minutes, the original measurements were averaged and resampled into daily data. If there were missing data for some hours of a day, we eliminate that day and denoted the missing data with a null value. To estimate active layer thickness (ALT), we applied linear interpolation to the temperature-depth profiles from 2011 to 2020 at the permafrost sites (Table 6).

Table 6 The proportion of missing soil temperature (ST) and volumetric water content (VWC) data at each site.

Site	Proportion of Missing Data (%)	
	ST	VWC
EBoA	7.1	7.1
EBoB	2.8	2.8
PT1	10.4	10.4
PT3	26.7	26.7
PT4	13.4	13.4
PT5	9.6	9.6
PT6	25.5	42.2
PT9	6.7	6.7
PT10	26.7	28.3

https://doi.org/10.5194/essd-2022-347
Preprint. Discussion started: 23 November 2022

Mean annual ground temperature (MAGT) at the depth of zero annual amplitude (ZAA)—the depth at which seasonal changes in temperature are ≤0.1 °C—is always used to represent permafrost thermal dynamics. Here, we use the observations at each borehole to estimate the ZAA, and find that it varies between 16.0 and 18.0 m. Thus, MAGT at 16.0 m depth (denoted as MAGT_16) is chosen to determine the thermal characteristics and permafrost dynamics. Permafrost thickness was obtained through linear interpolation of the temperature-depth profiles at the depth of 0 °C (Cao et al., 2018).

For the long-term analyses of climate, active layer, and permafrost temperature changes, we used linear regression with a 95% confidence interval. To reduce the uncertainties, the linear trend was not estimated for the length of data less than 5 years in each borehole.

3.2 Experimental analysis of soil carbon

Soil organic carbon (SOC) is based on homogenized samples that were quantified using dry combustion on a vario EL elemental analyzer (Elemental, Hanau, Germany). For this process, 0.5 g dry soil samples were pretreated with HCl (10 mL 1 mol L^{-1}) for 24 h to remove any carbonate. Bulk density (BD) was determined by measuring the volume (length, width, height) of a section of frozen core, and then drying the segment at 105°C (for 48 h) and determining its mass. Density of soil organic carbon (SOCD, kg m^{-2}) was calculated using Eq. (1) (Dörfer et al., 2013):

$$SOCD = C \times BD \times T \times (1-CF) \tag{1}$$

where C is the SOC content (wt %), BD the bulk density (g cm^{-3}), T the soil layer thickness, and CF any rock fragments (wt %).

3.3 Monitoring of ecosystem respiration rates and net ecosystem exchanges

CO_2 emission rates are monitored using a dark chamber to determine the ecosystem respiration rates (ERR). At the monitoring plots, NEE and ERR were measured during the growing seasons from 2015 to 2016. All ERR and NEE were measured three times and then averaged for each plot. ERR was measured using an LI-8100 Automated Soil CO_2 Flux System (Li-Cor Inc., Lincoln, NE, USA). PVC collars with a diameter of 20 cm were permanently inserted approximately 3.0 cm into

https://doi.org/10.5194/essd-2022-347
Preprint. Discussion started: 23 November 2022

the ground at each monitoring site in early May 2014. The ecosystem CO_2 fluxes that were obtained between 08:30 and 11:30 a.m. on clear days were considered representative of a one-day average flux, according to measurements of diurnal gas flux variation (Lu et al., 2013). The ecosystem carbon emissions at 10:00 a.m. were similar to the mean diurnal values from 8:00 to 20:00 for the three vegetation types, based on our measurements. Therefore, the CO_2 flux was measured randomly between 9:00 and 11:00 a.m. Measurements were run in five minutes segments at each monitoring site. Ecosystem carbon emissions in each chamber were measured continuously three times, and then averaged to obtain a mean flux value.

NEE was measured immediately after ERR at each site. We used a light sensor connected with an EGM-4 elemental gas analyzer (PP systems, Amesbury, MA, USA) to monitor solar radiation, to ensure the NEE measurements were obtained under similar radiation conditions during the field observations. If solar radiation decreased rapidly due to, e.g., a sudden appearance of clouds, the measurement would stop until radiation resumed. Acrylic glass frames (0.25 m × 0.25 m) were inserted at a depth of 3.0 cm in October 2014, before the NEE data collection. The slots on the upper rings of the frames provide flat surfaces for the installation of a clear chamber (0.25 m × 0.25 m × 0.25 m). The chamber was sealed to the frame using sealing film while measuring NEE. The air inside the chamber was mixed continuously by running two small fans. The chamber was connected to the LI-8100 via the designed inlet and outlet, using the plastic tubes of the LI-8100. NEE was then recalculated based on the volume of the chamber.

4 Data description

4.1 Meteorological data

The comprehensive meteorological systems illustrate that the meteorological variables undergo a strong annual cycle, as can be seen at, e.g., EBoA (Figure 5). Annual average temperatures are below 0 °C at all the five stations (Figure 6). The EBoA site has the highest annual average temperature of about −2.65 °C, followed by PT5 with −4.10°C, PT9 with −4.78°C, PT1 with −4.82°C, and PT6 with the lowest at approximately −5.29 °C. At the seasonal(from Mar. to May for spring, Jun. To Aug.

https://doi.org/10.5194/essd-2022-347
Preprint. Discussion started: 23 November 2022

For summer, Sep. To Nov. For autumn, Dec. To Feb. For winter) scale, the EBoA site has the highest average seasonal temperatures of −13.26 ℃ in spring, −5.47 ℃ in summer, 6.96 ℃ in autumn, and −5.03 ℃ in winter. The seasonal temperatures at EBoA since 2014 have ranged from −14.38 ℃ to −10.88 ℃ for spring, −7.15 ℃ to −3.83 ℃ for summer, 6.37 ℃ to 8.13 ℃ for autumn, and −5.67 ℃ to −4.38 ℃ for winter. The average seasonal temperatures at the other four sites, ordered from high to low, are: PT5, PT9, PT1, and PT6. Average total seasonal and annual precipitation at the five meteorological sites with complete records since 2014 (Figure 7) show similar characteristics at each site. Precipitation mainly occurs in summer (June to August). PT9 has the highest seasonal total precipitation of 339 mm in summer. The average total annual precipitation, ranked from high to low, are PT9 with 532 mm, EBoA with 418 mm, PT5 with 373 mm, PT1 with 336 mm, and PT6 with 209 mm.

https://doi.org/10.5194/essd-2022-347
Preprint. Discussion started: 23 November 2022

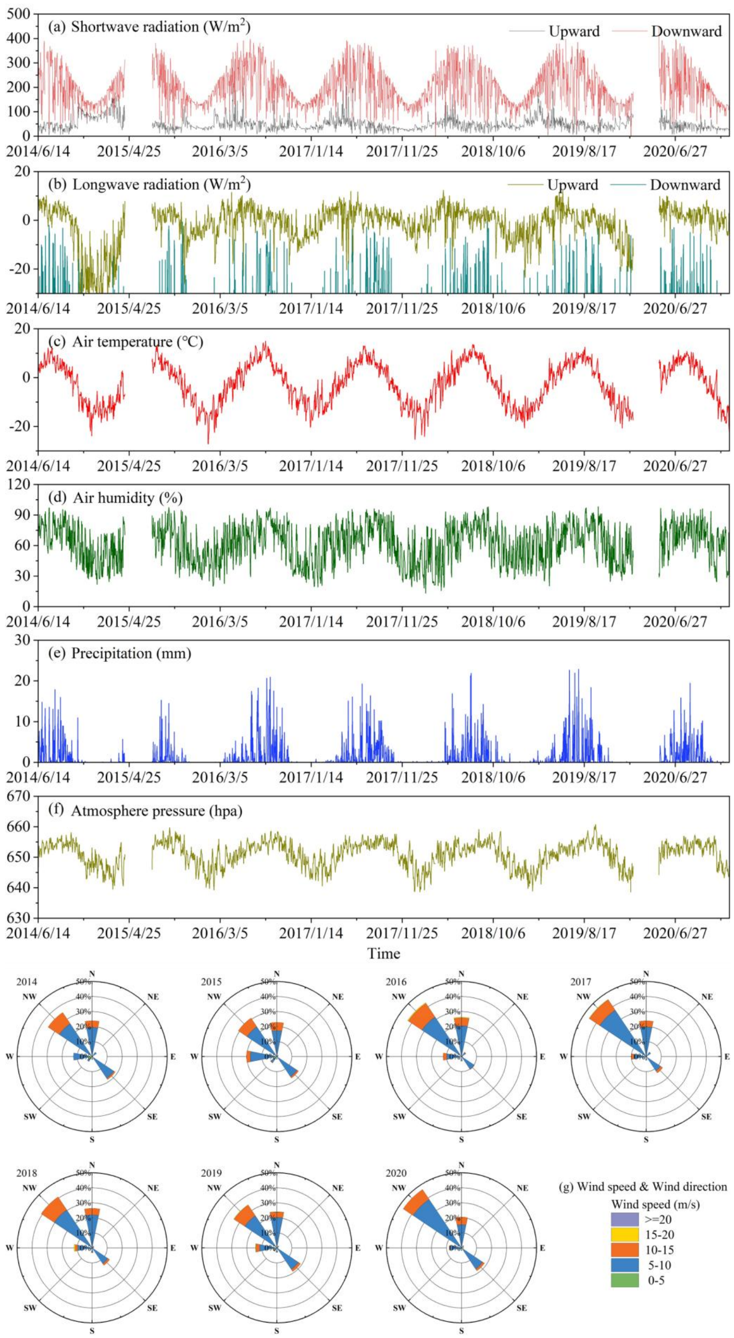

Figure 5 Observations of meteorological variables from 2014 to 2020 at EBoA including (a) shortwave radiation, (b) longwave radiation, (c) 2-m air temperature, (d) relative humidity, (e) precipitation, (f) atmosphere pressure, and (g) wind speed & direction.

https://doi.org/10.5194/essd-2022-347
Preprint. Discussion started: 23 November 2022

Open Access Earth System Science Data Discussions

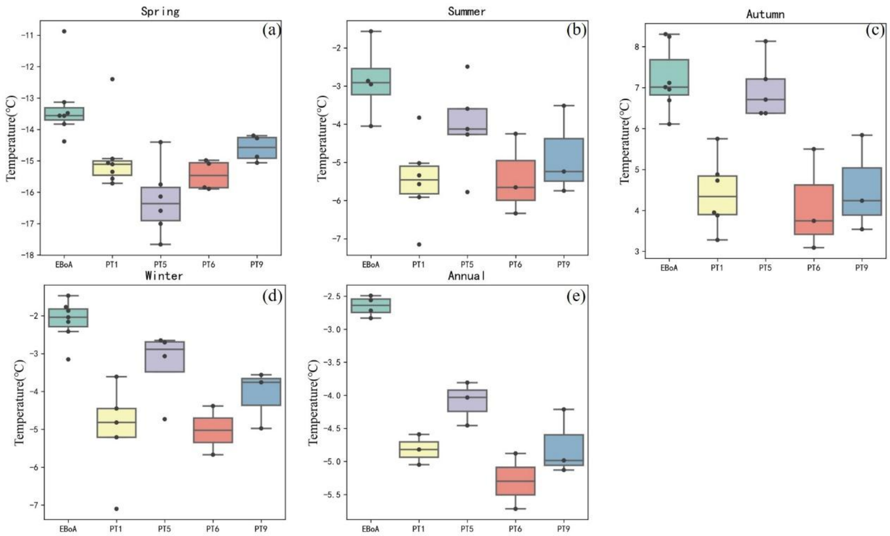

Figure 6 Box plots of average temperature observations for (a) spring, (b) summer, (c) autumn, (d) winter, and (e) annual.

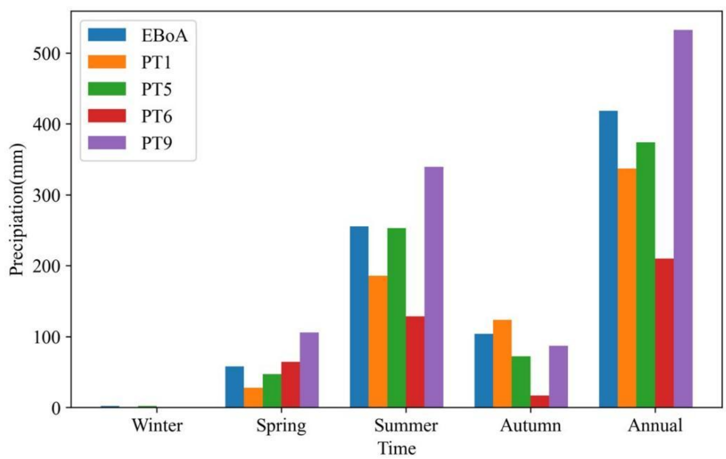

Figure 7 Seasonal and annual average precipitation at each site since 2014.

4.2 Active layer thickness and hydrothermal conditions

Based on soil temperature at each site, ALT ranges from less than 1.0 m to greater than 5.6 m in this study area (Table 7). The shallowest ALT of 0.77±0.05 m occurred at EBoA, and the deepest ALT of 5.64±0.60 m at site PT10 in the Yeniugou area. Time

https://doi.org/10.5194/essd-2022-347
Preprint. Discussion started: 23 November 2022

series of ALT indicate significant decreases at EBoA at a rate of −0.1 m/10 yr. At the other sites, ALT also increased significantly in recent years, the fastest at PT10 with a rate of 3.8 m/10 yr. Trends at the other sites ranged 0.1–0.8 m/10 yr.

Table 7 Active layer thickness at each site.

Site	ALT±STD (m)
EBoA	0.77±0.05
EBoB	0.91±0.06
PT1	1.84±0.03
PT2	1.57±0.03
PT3	2.02±0.17
PT4	3.53±0.18
PT5	3.70±0.26
PT6	2.52±0.26
PT7	3.09±0.07
PT9	1.97±0.19
PT10	5.64±0.60

The hydrothermal regime of the active layer is an important indicator for the response of frozen ground to climate change. We analyze the EBoA site to showcase the freeze-thaw process variability in our monitoring network. The soil temperature profile reflects the seasonal dynamics (Figure 8a): thawing onset is generally in mid-May, and the maximum thaw depth occurs in mid-October. Freezing from both directions begins thereafter, in early November.

The soil temperature amplitude in the active layer decreases rapidly with increasing soil depth. The minimum and maximum soil temperatures were −12.44 °C and 10.75 °C, respectively, at the 0.05 m depth, −11.36 °C and 9.22 °C at 0.1 m, −9.29 °C and 8.77 °C at 0.2 m, −7.35 °C and 3.79 °C at 0.4 m, −6.24 °C and 4.28 °C at 0.6 m, and −5.49 °C and 0.7 °C at the 0.77 m depth. The mean annual soil temperature during the 2012–2020 period was highest in 2016.

Soil moisture also clearly reflects the freeze-thaw cycle in the active layer (Figure 8b). In the thawing season, soil moisture decreases gradually with increasing depth. It was around 0.8 m^3/m^3 at the 0–20 cm depth, 0.5 to 0.6 m^3/m^3 at 20–40 cm depth, and 0.4 to 0.5 m^3/m^3 in the lower part of the active layer. During the freezing season, soil moisture is substantially different: it is higher in the lower depths (0.2

https://doi.org/10.5194/essd-2022-347
Preprint. Discussion started: 23 November 2022

m^3/m^3) than in the upper portions (0–0.1 m^3/m^3) of the active layer, considering unfrozen water and the phase change in the freezing process.

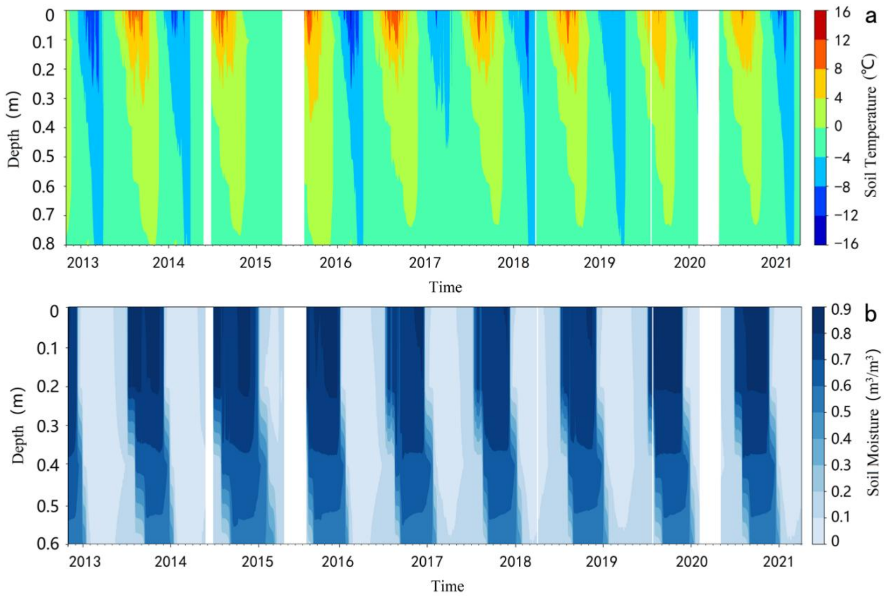

Figure 8 Variability of (a) soil temperature and (b) soil moisture at EBoA.

4.4 MAGT and permafrost thickness

The MAGT at 16.0 m depth (MAGT_16) ranged from −1.80±0.07 °C to 2.28±0.04 °C at the observing sites (Figure 9 and Table 8). MAGT_16 was less than −1 °C at five sites (PT1, PT3, PT6, PT7, and PT9), and greater than 0 °C at six sites (PT5, PT10, PT12, SFGT, SFGT5, and SFGT6). Increasing MAGT_16 was found at most of the sites, with trends ranging −0.02–0.28°C/10 yr. In cold permafrost MAGT_16 increases faster than in warmer permafrost. For example, the fastest increase occurred at PT1, the coldest permafrost site, where MAGT_16 has increased 0.28 °C/10 yr since 2012. There is no statistically significant trend at PT4 or PT9, and even a slight decrease in permafrost temperature at the PT8 site. MAGT_16 changes at most sites range 0.1–0.2 °C/10 yr. For SFG, MAGT_16 at SFGT6 increases at 0.18 °C/10 yr.

https://doi.org/10.5194/essd-2022-347
Preprint. Discussion started: 23 November 2022

Based on ground temperature, permafrost thickness ranges from 8.25 m to 206.29 m. Thicker permafrost was found at high elevation, e.g., the PT1 and PT7 sites. Although elevation at EBoA and EBoB is lower than at PT1 and PT7, permafrost thickness was about 80.0 m. This could be explained by the peat layer and high ground ice content at those sites, which can insulate the permafrost (Du et al., 2022).

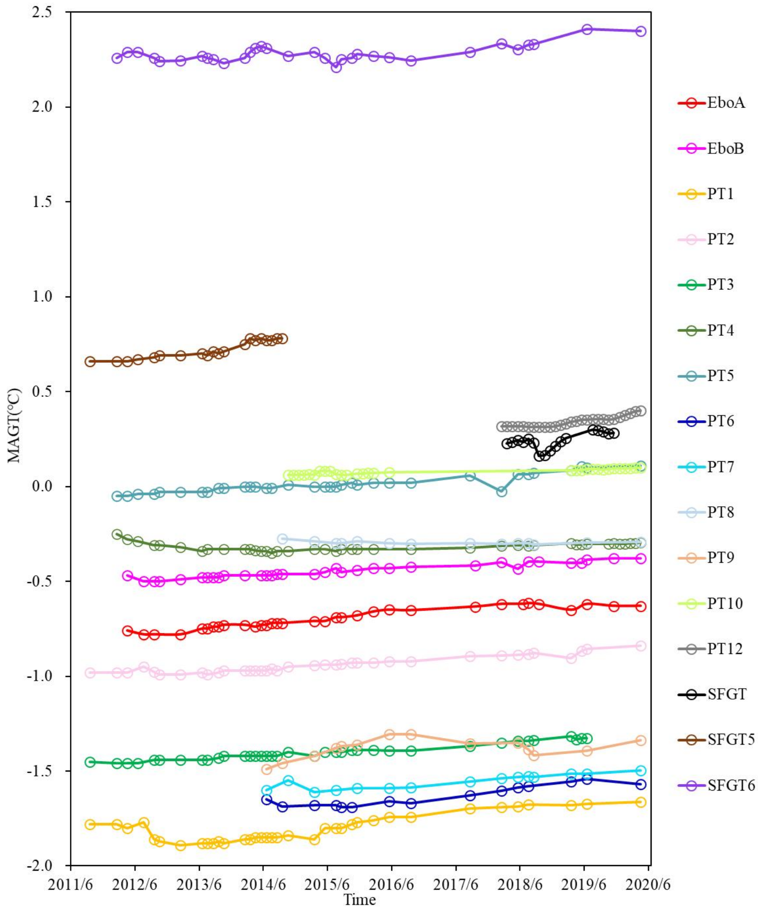

Figure 9 Changes in mean annual ground temperature at 16.0 m depth at each site during the observational time period.

Table 8 Changes of MAGT_16 and permafrost thickness at each site. Asterisks indicate statistically significant (95% confidence level) trends; NaN indicates missing values.

Site	MAGT_16 (℃)	Slope (℃/10yr)	Permafrost thickness (m)

https://doi.org/10.5194/essd-2022-347
Preprint. Discussion started: 23 November 2022

EBoA	−0.70±0.05	0.20*	88.00
EBoB	−0.45±0.04	0.14*	82.00
PT1	−1.80±0.07	0.28*	107.14
PT2	−0.94±0.04	0.18*	62.49
PT3	−1.40±0.04	0.18*	90.08
PT4	−0.32±0.02	0.02	26.50
PT5	0.01±0.04	0.18*	16.55
PT6	−1.63±0.05	0.23*	133.75
PT7	−1.56±0.04	0.17*	206.29
PT8	−0.30±0.01	−0.02	25.16
PT9	−1.38±0.05	0.11	87.03
PT10	0.08±0.01	0.06*	14.30
PT12	0.34±0.03	NAN	8.25
SFGT	0.24±0.04	NAN	NAN
SFGT5	0.72±0.05	NAN	NAN
SFGT6	2.28±0.04	0.18*	NAN

4.6 Soil organic carbon content

The distribution of SOC densities varies among different vegetation types and soil depths (Figure 10). The SOC densities at PT9 and EboA with AWM vegetation type were much higher than at sites EboB, PT4, PT5, PT6, and PT7 where the vegetation type is AM. The mean SOC densities of the sites ranges from 0.40 to 22.41 kg m^{-3}, with the highest values occurring at sites with AWM vegetation. The lowest SOC densities were recorded at the sites with AS vegetation (PT10, PT11 and PT12), and the mean values of AS were less than 1.0 kg m^{-3}.

For all the measured samples, the C/N ratios ranged from 2.02 to 73.04 (Figure 10). The variability of C/N ratios with depth follows a similar trend as the SOC densities at sites PT4–PT7. The average C/N ratio values at the permafrost boreholes were 19.98, 17.65, 13.61, and 13.44 for the PT4, PT5, PT6, and PT7 sites, respectively. The C/N ratios for PT9, EboA, and EboB were 11.03, 7.59, and 6.45 in AWM areas.

https://doi.org/10.5194/essd-2022-347
Preprint. Discussion started: 23 November 2022

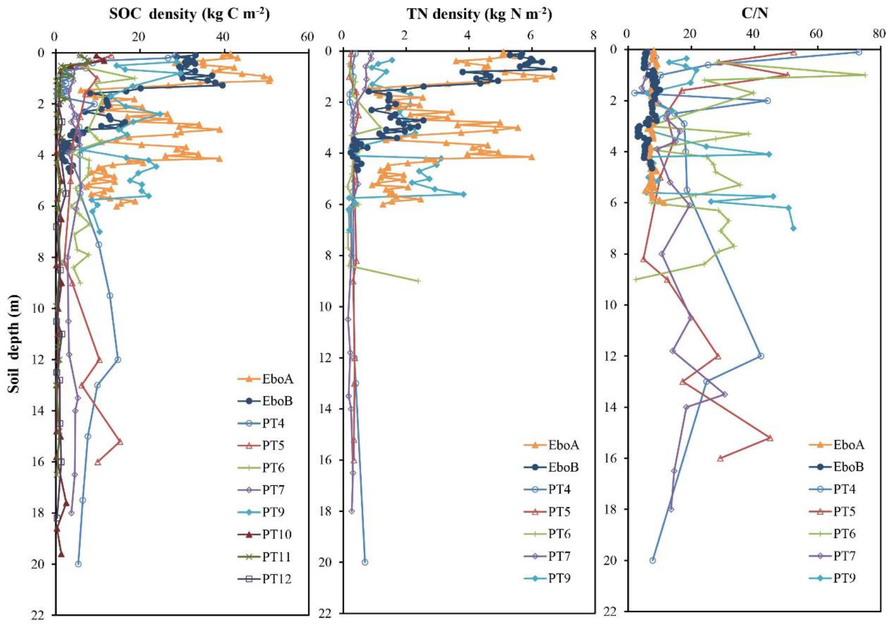

Figure 10 The distribution of soil organic carbon (SOC) density, total nitrogen (TN) density, and C/N ratio at the boreholes.

4.7 Ecosystem carbon emission rates

The ERRs at both sites increased from June to a maximum in July and August, and then decreased in September during 2014–2016 (Figure 11). At the Ebo sites, the ERR in the AWM region (EboA site, average of 3.63 μmol CO_2 m^{-2} s^{-1}) was lower than in the AM region (EboB site, average of 5.79 μmol CO_2 m^{-2} s^{-1}). The mean ERR at the AWM sites (PT1, PT2, and PT3) was 2.92 μmol CO_2 m^{-2} s^{-1}. The ERR was similar at both PT4 and PT5 in AM vegetation, with an average value of 3.15 μmol CO_2 m^{-2} s^{-1}. At the AS sites (SFG1, SFG2, and SFG3), the mean ERR was 4.11 μmol CO_2 m^{-2} s^{-1}.

https://doi.org/10.5194/essd-2022-347
Preprint. Discussion started: 23 November 2022

Open Access Earth System Science Data Discussions

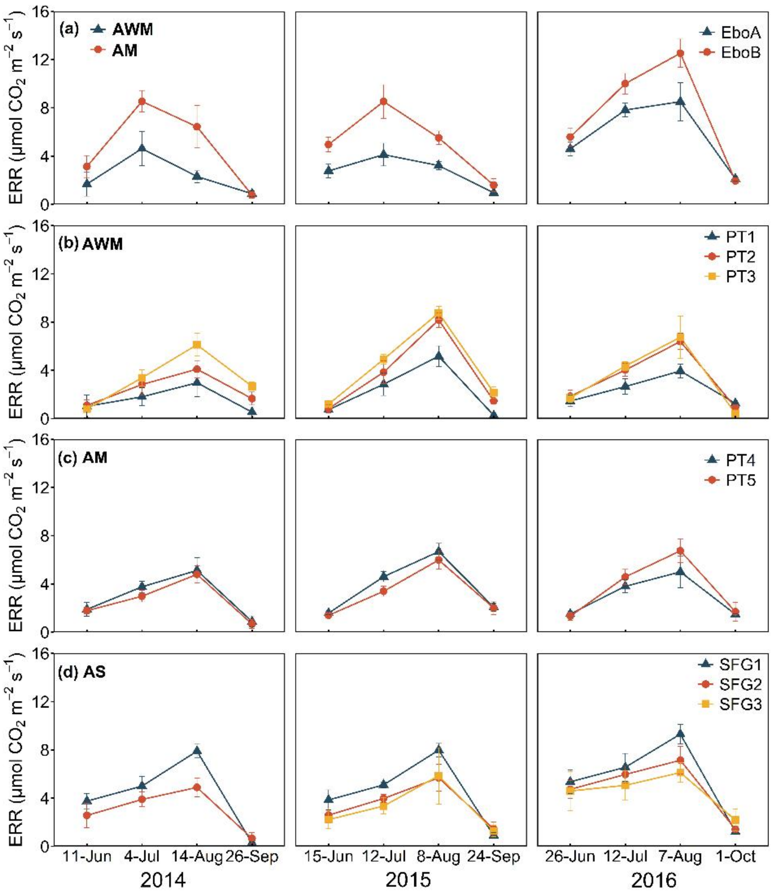

Figure 11 Ecosystem respiration rates (ERR) in different vegetation types during the growing seasons from 2014 to 2016.

The ERR in AWM ranged from 1.1 to 7.5 μmol CO_2 m^{-2} s^{-1} in the monitoring plots (Figure 12). Meanwhile, ERR in AM ranged from 1.4 to 9.5 μmol CO_2 m^{-2} s^{-1}. The average NEE in AWM (EboA) was −2.02 μmol CO_2 m^{-2} s^{-1} (Figure 13). The NEE at the AM sites (EboB and PT5) was −2.60 to −1.72 μmol CO_2 m^{-2} s^{-1}. All NEE data for these boreholes are shown in Table 9.

https://doi.org/10.5194/essd-2022-347
Preprint. Discussion started: 23 November 2022

Open Access Earth System Science Data Discussions

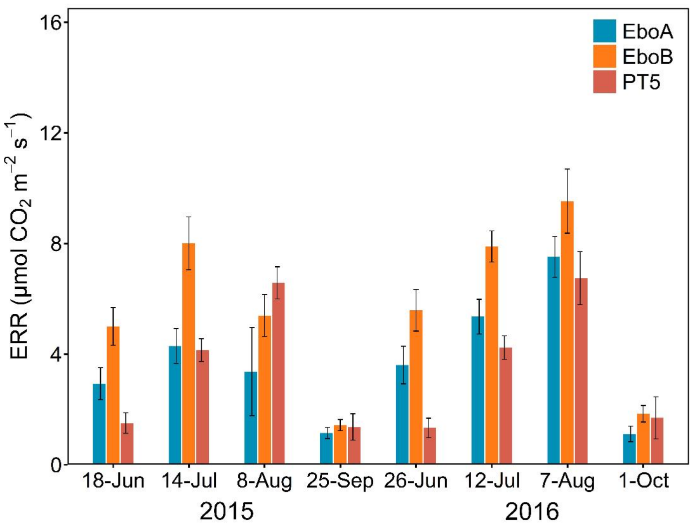

Figure 12 Ecosystem respiration rates (ERR) in alpine wet meadow (AWM, EboA) and alpine meadow (AW, EboB, and PT5) during the 2015 and 2016 growing seasons.

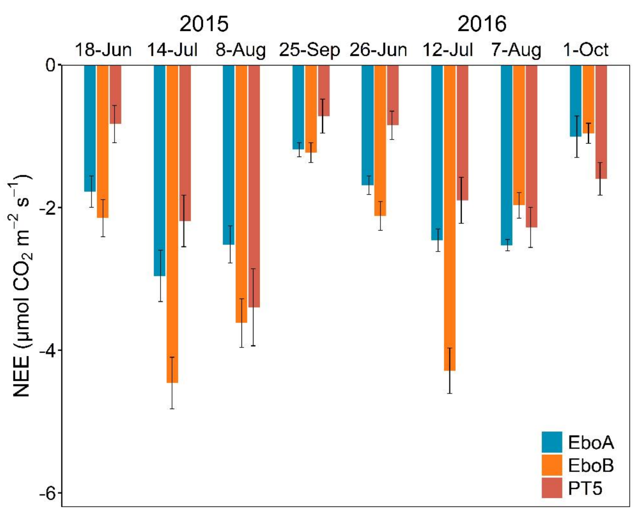

Figure 13 Net ecosystem exchange (NEE) in alpine wet meadow (AWM, EboA) and alpine meadow (AW, EboB, and PT5) during the 2015 and 2016 growing seasons.

Table 9. Net ecosystem exchange (NEE) at EboA, EboB, and PT5 sites during the growing seasons.

https://doi.org/10.5194/essd-2022-347
Preprint. Discussion started: 23 November 2022

NEE (μmol CO_2 m^{-2} s^{-1})			
Period	EboA	EboB	PT5
2015-18-Jun	−1.78±0.22	−2.15±0.26	−0.83±0.26
2015-14-Jul	−2.96±0.36	−4.46±0.36	−2.19±0.36
2015-8-Aug	−2.52±0.26	−3.62±0.34	−3.40±0.54
2015-25-Sep	−1.19±0.10	−1.23±0.14	−0.72±0.24
2016-26-Jun	−1.69±0.13	−2.12±0.20	−0.85±0.20
2016-12-Jul	−2.46±0.16	−4.29±0.32	−1.90±0.32
2016-7-Aug	−2.53±0.08	−1.97±0.18	−2.28±0.28
2016-1-Oct	−1.01±0.29	−0.96±0.14	−1.60±0.23

5 Data availability

All datasets described in this paper have been released and can be freely downloaded from the National Tibetan Plateau/Third Pole Environment Data Center (http://dx.doi.org/10.11888/Cryos.tpdc.272840, Mu and Peng, 2022).

6 Conclusions

Comprehensive monitoring networks of frozen ground and soil carbon were installed in the upper reaches of the Heihe River Basin in the Qilian Mountains, where meteorological indicators, seasonal frozen ground, active layer, permafrost, and soil carbon data are automatically measured. These observational data are intended for studies on land-atmosphere interactions, permafrost response to climate change, and carbon changes in different vegetation types. These high-quality, long-term observations can be used to estimate permafrost degradation, for global earth system model validation, and permafrost-carbon dynamics.

Author contributions. CM, XP and TZ designed the research and obtained funding. RD, BL, HJ, HL, MM analyzed the data and prepared the data files. WS, FC, and XP conducted the field work. CM, XP, OWF, XW wrote the paper with input from the coauthors and coordinated the analysis and contributions from all coauthors.

Competing interests. The contact author has declared that neither they nor their coauthors have any competing interests.

Disclaimer. Publisher's note: Copernicus Publications remains neutral with regard to jurisdictional claims in published maps and institutional affiliations.

Acknowledgements

This work was supported by the National Natural Science Foundation of China (42171120, 41871050, 42161160328), the Second Tibetan Plateau Scientific Expedition and Research Program (STEP) (2019QZKK0605, 2019QZKK0905), the Strategic Priority Research Program of Chinese Academy of Sciences (Grant No. XDA20100103), and the Fundamental Research Funds for the Central Universities (lzujbky-2021-ct13).

References:

Biskaborn, B. K., Smith, S. L., Noetzli, J., Matthes, H., Vieira, G., Streletskiy, D. A., Schoeneich, P., Romanovsky, V. E., Lewkowicz, A. G., Abramov, A., Allard, M., Boike, J., Cable, W. L., Christiansen, H. H., Delaloye, R., Diekmann, B., Drozdov, D., Etzelmüller, B., Grosse, G., Guglielmin, M., Ingeman-Nielsen, T., Isaksen, K., Ishikawa, M., Johansson, M., Johannsson, H., Joo, A., Kaverin, D., Kholodov, A., Konstantinov, P., Kröger, T., Lambiel, C., Lanckman, J.-P., Luo, D., Malkova, G., Meiklejohn, I., Moskalenko, N., Oliva, M., Phillips, M., Ramos, M., Sannel, A. B. K., Sergeev, D., Seybold, C., Skryabin, P., Vasiliev, A., Wu, Q., Yoshikawa, K., Zheleznyak, M., and Lantuit, H.: Permafrost is warming at a global scale, Nature Communications, 10, 10.1038/s41467-018-08240-4, 2019.

Cao, B., Zhang, T. J., Peng, X. Q., Mu, C. C., Wang, Q. F., Zheng, L., Wang, K., and Zhong, X. Y.: Thermal Characteristics and Recent Changes of Permafrost in the Upper Reaches of the Heihe River Basin, Western China, Journal of Geophysical Research: Atmospheres, 123, 7935-7949, 10.1029/2018JD028442, 2018.

Cheng, G. D., Zhao, L., Li, R., Wu, X. D., Sheng, Y., Hu, G. J., Zou, D. F., Jin, H. J., Li, X., and Wu, Q. B.: Characteristic, changes and impacts of permafrost on Qinghai-Tibet Plateau, Chinese Science Bulletin-Chinese, 64, 2783-2795, 10.1360/tb-2019-0191, 2019.

Dörfer, C., Kühn, P., Baumann, F., He, J.-S., and Scholten, T.: Soil organic carbon pools and stocks in permafrost-affected soils on the tibetan plateau, PLoS One, 8, e57024-e57024, 10.1371/journal.pone.0057024, 2013.

Ding, Y., Zhang, S., Zhao, L., Li, Z., and Kang, S.: Global warming weakening the

https://doi.org/10.5194/essd-2022-347
Preprint. Discussion started: 23 November 2022

inherent stability of glaciers and permafrost, Science Bulletin, 64, 245-253, doi.org/10.1016/j.scib.2018.12.028, 2019.

Du, R., Peng, X., Frauenfeld, O., Sun, W., Liang, B., Chen, C., Jin, H., and Zhao, Y.: The role of peat on permafrost thaw based on field observations, CATENA, 208, 105772, 10.1016/j.catena.2021.105772, 2022.

Guo, D., Wang, H., and Li, D.: A projection of permafrost degradation on the Tibetan Plateau during the 21st century, Journal of Geophysical Research Atmospheres, 117, 2012.

Hu, G., Zhao, L., Li, R., Wu, X., Wu, T., Xie, C., Zhu, X., and Su, Y.: Variations in soil temperature from 1980 to 2015 in permafrost regions on the Qinghai-Tibetan Plateau based on observed and reanalysis products, Geoderma, 337, 893-905, 10.1016/j.geoderma.2018.10.044, 2019.

Hu, G., Zhao, L., Wu, X., Li, R., Wu, T., Xie, C., Pang, Q., Xiao, Y., Li, W., Yongping, Q., and Shi, J.: Modeling permafrost properties in the Qinghai-Xizang (Tibet) Plateau, Science China Earth Sciences, 58, https://doi.org/10.1007/s11430-015-5197-0, 2015.

Huang, L., Liu, L., Jiang, L., and Zhang, T.: Automatic Mapping of Thermokarst Landforms from Remote Sensing Images Using Deep Learning: A Case Study in the Northeastern Tibetan Plateau, Remote Sensing, 10, 10.3390/rs10122067, 2018.

Hugelius, G., Strauss, J., Zubrzycki, S., Harden, J. W., Schuur, E. A. G., C.-L., P., Schirrmeister, L., Grosse, G., Michaelson, G. J., and Koven, C. D.: Estimated stocks of circumpolar permafrost carbon with quantified uncertainty ranges and identified data gaps, Biogeosciences, 11, 6573– 6593, 2014.

James, M., Lewkowicz, A. G., Smith, S. L., and Miceli, C. M.: Multi-decadal degradation and persistence of permafrost in the Alaska Highway corridor, northwest Canada, Environmental Research Letters, 8, 045013, 2013.

Koven, C. D., Riley, W. J., and Stern, A.: Analysis of permafrost thermal dynamics and response to climate change in the CMIP5 Earth System Models, Journal of Climate, 26, 1877-1900, 2013.

Lawrence, D. M. and Slater, A. G.: A projection of severe near-surface permafrost degradation during the 21st century, Geophysical Research Letters, 32, 2005.

Lu, X., Fan, J., Yan, Y., and Wang, X.: Responses of soil CO2 fluxes to short-term experimental warming in alpine steppe ecosystem, Northern Tibet, PLoS One, 8, e59054-e59054, 10.1371/journal.pone.0059054, 2013.

Marchuk, G. I.: Methods of numerical mathematics, Springer-Verlag, New York1975.

McGuire, A. D., Lawrence, D. M., Koven, C., Clein, J. S., Burke, E., Chen, G., Jafarov, E., MacDougall, A. H., Marchenko, S., and Nicolsky, D.: Dependence of the evolution of carbon dynamics in the northern permafrost region on the trajectory of climate change, Proceedings of the National Academy of Sciences, 115, 3882-3887, 2018.

Mu, C. and Peng, X.: A synthesis dataset of frozen ground and soil carbon in Heihe River Basin Qilian Mountainous (2011－2020). National Tibetan Plateau Data Center [data set], http://dx.doi.org/10.11888/Cryos.tpdc.272840, 2022.

Mu, C., Zhang, T., Zhang, X., Cao, B., and Peng, X.: Sensitivity of soil organic matter decomposition to temperature at different depths in permafrost regions on the northern Q inghai-T ibet P lateau, European journal of soil science, 67, 773-781, 2016.

Mu, C., Zhang, T., Cao, B., Wan, X., Peng, X., and Cheng, G.: Study of the organic carbon storage in the active layer of the permafrost over the Eboling Mountain in the upper reaches of the Heihe River in the Eastern Qilian Mountains Journal of Glaciology and Geocryology, 35, 1-9, 2013.

Mu, C., Zhang, T., Zhao, Q., Su, H., Wang, S., Cao, B., Peng, X., Wu, Q., and Wu, X.: Permafrost affects carbon exchange and its response to experimental warming on the northern Qinghai-Tibetan Plateau, Agricultural & Forest Meteorology, 247, 252-259, 2017.

Mu, C., Shang, J., Zhang, T., Fan, C., Wang, S., Peng, X., Zhong, W., Zhang, F., Mu, M., and Jia, L.: Acceleration of thaw slump during 1997–2017 in the Qilian Mountains of the northern Qinghai-Tibetan plateau, Landslides, 17, 1051-1062, 2020a.

Mu, C., Zhang, T., Wu, Q., Cao, B., Zhang, X., Peng, X., Wan, X., Zheng, L., Wang, Q., and Cheng, G.: Carbon and Nitrogen Properties of Permafrost over the Eboling Mountain in the Upper Reach of Heihe River Basin, Northwestern China, Arctic, Antarctic, and Alpine Research, 47, 203-211, https://doi.org/10.1657/AAAR00C-13-095, 2015.

Mu, C., Abbott, B., Norris, A., Mei, M., Fan, C., Chen, X., Jia, L., Yang, R., Zhang, T., Wang, K., Peng, X., Wu, Q., Guggenberger, G., and Wu, X.: The status and stability of permafrost carbon on the Tibetan Plateau, Earth-Science Reviews, 211, 10.1016/j.earscirev.2020.103433, 2020b.

Obu, J., Westermann, S., Bartsch, A., Berdnikov, N., Christiansen, H. H., Dashtseren, A., Delaloye, R., Elberling, B., Etzelmüller, B., Kholodov, A., Khomutov, A., Kääb, A., Leibman, M. O., Lewkowicz, A. G., Panda, S. K., Romanovsky, V., Way, R. G., Westergaard-Nielsen, A., Wu, T., Yamkhin, J., and Zou, D.: Northern Hemisphere permafrost map based on TTOP modelling for 2000–2016 at 1 km2 scale, Earth-Science Reviews, 193, 299-316, https://doi.org/10.1016/j.earscirev.2019.04.023, 2019.

Peng, X., Zhang, T., Cao, B., Wang, Q., Wang, K., Shao, W., and Guo, H.: Changes in Freezing-Thawing Index and Soil Freeze Depth Over the Heihe River Basin, Western China, Arctic Antarctic and Alpine Research, 48, 161-176, 10.1657/AAAR00C-13-127, 2016.

Peng, X., Zhang, T., Frauenfeld, O., Wang, K., Luo, D., Cao, B., Hang, s., Jin, H., and Wu, Q.: Spatiotemporal Changes in Active Layer Thickness under Contemporary and Projected Climate in the Northern Hemisphere, Journal of Climate, 31, 251-266, 10.1175/JCLI-D-16-0721.1, 2018.

Romanovsky, V. E., Drozdov, D. S., Oberman, N. G., Malkova, G. V., Kholodov, A. L., Marchenko, S. S., Moskalenko, N. G., Sergeev, D. O., Ukraintseva, N. G., and Abramov, A. A.: Thermal state of permafrost in Russia, Permafrost & Periglacial Processes, 21, 136-155, 2010.

Schuur, E. A. G., McGuire, A. D., Schädel, C., Grosse, G., Harden, J. W., Hayes, D. J., Hugelius, G., Koven, C. D., Kuhry, P., Lawrence, D. M., Natali, S. M., Olefeldt, D., Romanovsky, V. E., Schaefer, K., Turetsky, M. R., Treat, C. C., and Vonk, J. E.: Climate change and the permafrost carbon feedback, Nature, 520, 171-179, 10.1038/nature14338, 2015.

Slater, A. G. and Lawrence, D. M.: Diagnosing present and future permafrost from climate models, Journal of Climate, 26, 5608-5623, 2013.

Smith, S. L., O'Neill, H. B., Isaksen, K., Noetzli, J., and Romanovsky, V. E.: The changing thermal state of permafrost, Nature Reviews Earth & Environment, 3, 10-23, 2022.

Yao, T. D., Y., Shilong, P., Miaogen, S., Jing, G., Wei, Y., Guoqing, Z., Yanbin, L., Yang, G., Liping, Z., and Baiqing, X.: Chained impacts on modern environment of interaction between Westerlies and Indian Monsoon on Tibetan Plateau, Bulletin of Chinese Academy of Sciences (Chinese Version), 32, 976-984, 2017.

Turetsky, M. R., Abbott, B. W., Jones, M. C., Anthony, K. W., Olefeldt, D., Schuur, E. A. G., Grosse, G., Kuhry, P., Hugelius, G., Koven, C., Lawrence, D. M., Gibson, C., Sannel, A. B. K., and McGuire, A. D.: Carbon release through abrupt permafrost thaw, Nature Geoscience, 13, 138-143, 10.1038/s41561-019-0526-0, 2020.

Vaks, A., Mason, A. J., Breitenbach, S. F. M., Kononov, A. M., Osinzev, A. V., Rosensaft, M., Borshevsky, A., Gutareva, O. S., and Henderson, G. M.: Palaeoclimate evidence of vulnerable permafrost during times of low sea ice, Nature, 577, 221-225, 10.1038/s41586-019-1880-1, 2020.

Wang, K., Jafarov, E., and Overeem, I.: Sensitivity evaluation of the Kudryavtsev permafrost model, Science of The Total Environment, 720, 137538, 10.1016/j.scitotenv.2020.137538, 2020.

Wang, Q., Zhang, T., Peng, X., Cao, B., and Wu, Q.: Changes of soil thermal regimes in the Heihe River Basin over Western China, Arctic, Antarctic, and Alpine Research, 47, 231-241, 2015.

Yang, M., Wang, X., Pang, G., Wan, G., and Liu, Z.: The Tibetan Plateau cryosphere: Observations and model simulations for current status and recent changes, Earth-Science Reviews, 190, 353-369, https://doi.org/10.1016/j.earscirev.2018.12.018, 2019.

Zhao, C., Nan, Z., and Cheng, G.: Methods for modelling of temporal and spatial distribution of air temperature at landscape scale in the southern Qilian mountains, China, Ecological Modelling, 189, 209-220, 10.1016/j.ecolmodel.2005.03.016, 2005.

Zhao, L., Zou, D., Hu, G., Wu, T., Du, E., Liu, G., Xiao, Y., Li, R., Pang, Q., and Qiao, Y.: A synthesis dataset of permafrost thermal state for the Qinghai–Tibet (Xizang) Plateau, China, Earth System Science Data, 13, 4207-4218, 2021.

Zhao, L., Wu, X., Wang, Z., Sheng, Y., Fang, H., Zhao, Y., Hu, G., Li, W., Pang, Q., Shi, J., Mo, B., Wang, Q., Ruan, X., Li, X., and Ding, Y.: Soil organic carbon and total nitrogen pools in permafrost zones of the Qinghai-Tibetan Plateau, Scientific Reports, 8, 3656, 10.1038/s41598-018-22024-2, 2018.

Zou, D., Zhao, L., Sheng, Y., Chen, J., Hu, G., Wu, T., Wu, J., Xie, C., Wu, X., Pang, Q., Wang, W., Du, E., Li, W., Liu, G., Li, J., Qin, Y., Qiao, Y., Wang, Z., Shi, J., and

https://doi.org/10.5194/essd-2022-347
Preprint. Discussion started: 23 November 2022

Cheng, G.: A new map of permafrost distribution on the Tibetan Plateau, The Cryosphere, 11, 2527-2542, 10.5194/tc-11-2527-2017, 2017.